Thermoradiative devices enabled by hyperbolic phonon polaritons at nanoscales

Dudong Feng [a,b,*], Xiulin Ruan [b], Shannon K. Yee [a], Zhuomin M. Zhang [a,**]

[a] *George W. Woodruff School of Mechanical Engineering, Georgia Institute of Technology, Atlanta, GA 30332, USA*
[b] *School of Mechanical Engineering and the Birck Nanotechnology Center, Purdue University, West Lafayette, IND 47907, USA*

ABSTRACT

Thermoradiative (TR) devices, though proposed a decade ago, have seen little investigation due to their low-performance compared to other solid-state energy conversion technologies. Herein, we propose an InSb-hBN TR device with a nanoscale vacuum gap down to 10 nm that has the potential to achieve efficient waste heat recovery using solid-state technologies. By coupling the hyperbolic phonon polaritons of hBN with the interband transition of InSb, this TR device design can achieve an output power nearly 4 orders-of-magnitude higher than far-field scenarios and an upper bound efficiency up to 80% of the Carnot limit corresponding to only considering radiative loss. A detailed balance model combined with fluctuational electrodynamics for a multilayered anisotropic structure is developed to theoretically estimate the performance of TR devices from far- to near-field regime. Nonradiative losses are also investigated to elucidate their effects on performance. This work helps deepen the understanding of TR devices and provides a promising pathway to efficient low-grade (< 600 K) heat recovery.

1. Introduction

Thermoradiative (TR) cells generate electrical current by rejecting heat to cold surroundings through thermal radiation. Like other radiative energy converters, TR cells are usually made of semiconductor materials with a *pn* diode structure [1,2]. When the *pn* diode contacts with a local heat source, the thermally excited electrons and holes recombine and emit photons to the environment or a cold object. The free carrier population drops below the equilibrium value and results in a negative biased voltage, which can drive the free carriers in a circuit and generate electricity [3]. Santhanam and Fan [4] experimentally validated the concept of TR cell with a commercial photodiode soon after Byrnes et al. [5] proposed the idea in 2014. Field test of harvesting the power from the deep space was done by Ono et al. [6] with an improved power compared to the previous result of a proof-of-concept experiment [4]. Based on the theoretical analysis, TR cell can harvest waste heat more efficiently from a lower temperature range (e.g., 300–600 K) compared to other solid-state energy conversion technologies, such as thermoelectrics [7], and thermophotovoltaics (TPVs) [8,9].

Near-field radiation can greatly boost the performance of TPV and

TR devices [1,2]. However, few studies have been conducted on near-field TR devices [10]. Hsu et al. [11] first proposed an InSb-CaCO₃ near-field TR device with only 0.5% efficiency at 500 K when non-radiative losses are considered. Wang et al. [12] made the attempt to improve the performance of a near-field InAs TR cell with a ZrC grating. An artificial hyperbolic metamaterial made of ZrC and SiO₂ was designed by Ghanekar et al. [13] to support hyperbolic modes, which allow for extra photon transmission channels for the InAs TR cell. Lin et al. [14] indicated that by properly choosing the resonant frequencies supported by the receiver, Drude and Lorentz materials can provide descent enhancements on the power density and efficiency of an InAs TR cell. However, as a preliminary work on near-field TR devices, the materials properties were manually tuned without practical consideration [14].

Inspired by the early works on the near-field TPV [15] and TR [14], matching the optical phonon frequency of the emitter/receiver with the bandgap of radiative energy converters can provide ample enhancements on the power density and efficiency. As a natural hyperbolic metamaterial [16,17], hexagonal boron nitride (hBN) possesses almost the highest optical phonon frequency (~0.17 eV), which can perfectly
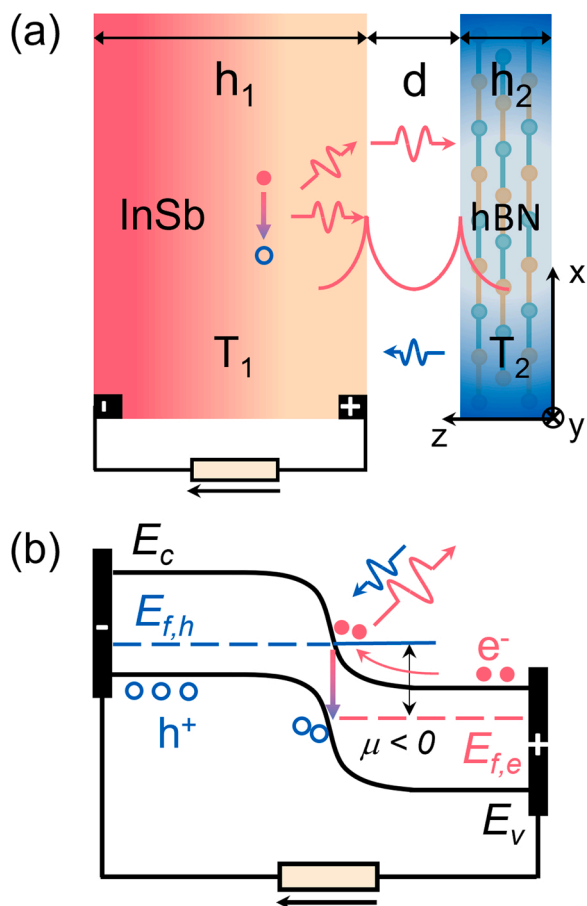

Fig. 1. (a) Schematic of the near-field TR device with an InSb cell and a hBN sheet at temperatures of T_1 and T_2, and with thickness of h_1 and h_2, respectively, separated by a vacuum gap of distance, d. (b) The band diagram of a TR cell. Here, E_c and E_v stand for the conduction and valance band, respectively. The photon chemical potential is equal to the difference between the quasi-Fermi levels of electrons (e⁻) and holes (h⁺), i.e., $\mu = E_{f,e} - E_{f,h}$.

match with the bandgap energy of InSb above room temperature. This indicates that hyperbolic phonon polaritons (HPhPs) can be excited within the narrow hyperbolic bands at the near-field regime. Therefore, the InSb-hBN thin-film structure can generate an ideal spectrum for radiative energy converters. Some researchers have proposed a near-field TPV device made of hBN-InSb with graphene covered on the TPV cell [18] or the hBN emitter [19]. However, all TPV and TR works mentioned above assumed a semi-infinite cell and neglected the non-radiative losses, which would substantially overestimate the performance of radiative energy converters.

In this work, we propose a near-field TR device using InSb-hBN with a thin-film structure. By combining the detailed balance analysis and fluctuational electrodynamics of anisotropic stratified media, this work accurately predicts the photogeneration and radiative recombination of a near-field TR device with finite thickness for the first time. Non-radiative losses and parasitic absorption are investigated, especially Auger generation at different temperatures. The vacuum gap thickness is varied to demonstrate the importance of HPhPs to the device performance. This proposed device structure provides a novel and efficient mechanism that makes TR devices a more competitive technology for waste heat recovery.

2. Methodology

As shown in Fig. 1(a), the near-field TR device is configured with an InSb TR cell of thickness h_1 and a hBN sheet with a thickness h_2 that acts
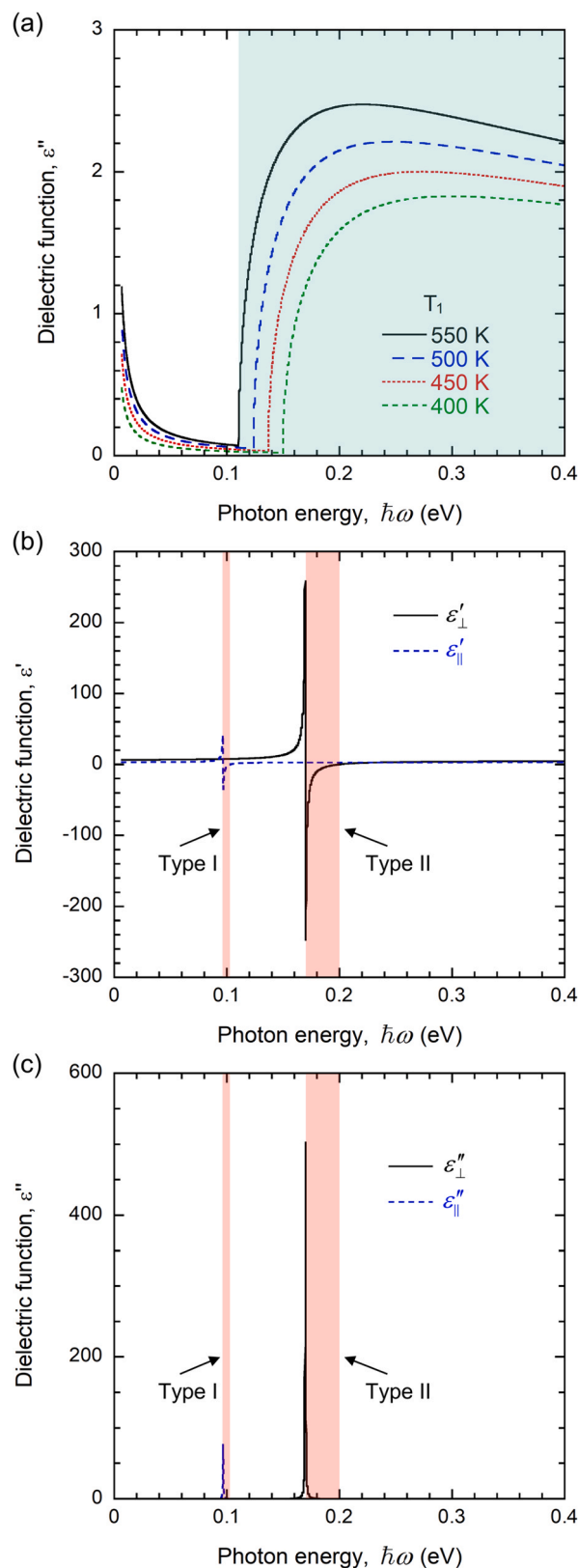
Fig. 2. (a) The imaginary part of the dielectric functions of InSb at different temperatures. The unshaded region and blue shaded region represent the below and above bandgap of InSb at 550 K, respectively. (b) The real part and (c) the imaginary part of the ordinary and extraordinary dielectric functions of hBN with two red shaded areas showing as hyperbolic bands.

as the receiver. A vacuum gap with the thickness of d is maintained between the two films so that both convection and conduction are forbidden. The InSb film and the hBN sheet are assumed to be individually at thermal equilibrium with T_1 and T_2 ($T_1 > T_2$), respectively. A thicker InSb film tends to have a higher possibility of nonradiative losses and parasitic absorption [11]. Therefore, the thickness of the InSb film (h_1) is fixed at 50 nm in this work.

The working principle of the near-field TR device can be considered as the optical and electrical processes separately, which are shown in Fig. 1(a) and (b), respectively. The thermally excited electrons and holes diffuse towards the depletion region and recombine to yield photon emission. As shown in Fig. 1(a), when the vacuum spacing is comparable or less the characteristic wavelength, near-field radiation can further enhance this photon emission by the coupling of HPhPs of the hBN sheet and interband transitions of the InSb cell. The photons emitted from the InSb cell can either propagate or tunnel through the vacuum gap to be absorbed by the hBN receiver. As depicted in Fig. 1(b), these enhanced radiative recombination of electron and hole pairs drive the quasi-Fermi levels of electrons and holes below the equilibrium states, which produces a negative chemical potential, μ. The remaining free carriers would overcome the junction voltage by diffusions resulting in a current to drive the external load. As the chemical potential is built up negatively, the free carriers can barely diffuse through the junction so that the photon emission is suppressed. The incoming photons from the environment or the cold object would reach an equilibrium with the emitted photons, as the open-circuit voltage is reached.

To calculate the radiation exchange between the InSb film and the hBN sheet, the dielectric function of undoped InSb is modeled as [20].

$$\varepsilon_I\left(\omega, T\right) = \left[m_1 + i\frac{\alpha(\omega, T)}{2k_0}\right]^2 \tag{1}$$

where m_1 is the refractive index, which is taken as a constant (3.96) at the investigated frequency range [21]. α is the absorption coefficient, which is approximately fit based on the experimental measurement at $T \leq 550$ K [22]:

$$\alpha(\omega, T) = \begin{cases} 0.4T - 120, & \omega < \omega_g(T) \\ \alpha_0\left[\frac{\omega - \omega_g(T)}{\omega_g(T)}\right]^{1/2}, & \omega \geq \omega_g(T) \end{cases} \tag{2}$$

where $\omega_g(T) = E_g(T)/\hbar$ is the angular frequency equivalent to the bandgap energy E_g and $\hbar$ is the reduced Planck constant. The bandgap energy of InSb monotonically decreases as temperature increases, which can be fitted with the Varshni relation [23,24]. The imaginary part of dielectric functions of InSb are plot for 400–550 K in Fig. 2(a), which reflects the strength of absorption/emission at a given frequency. For example, the bandgap of InSb is 0.11 eV at 550 K, the unshaded area is the frequency range which represents the parasitic absorption/emission, and the blue shaded area is the frequency range which represents the radiative recombination/generation.

The hBN sheet is an anisotropic material with the optical axis parallel to the z-direction. The dielectric tensor can be written as $\overline{\overline{\varepsilon}}_2 = \mathrm{diag}(\varepsilon_\perp, \varepsilon_\perp, \varepsilon_\parallel)$, where $\varepsilon_\perp$ and $\varepsilon_\parallel$ are the ordinary and extraordinary dielectric function, respectively. The dielectric function resulted from optical phonon resonance can be modeled with the Lorentz model and detailed information can be found in Ref. [24,25]. Type I ($\varepsilon'_\parallel < 0$ and $\varepsilon'_\perp > 0$) and Type II ($\varepsilon'_\parallel > 0$ and $\varepsilon'_\perp < 0$) hyperbolic bands are shaded with red color in Fig. 2(b) since these bands are the main heat transfer channels for near-field radiation. As show in Fig. 2(c), large imaginary part of dielectric function indicates strong resonances at the two optical phonon frequencies $\omega = 0.17$ eV and $\omega = 0.097$ eV for ordinary and extraordinary components. The overlap between the type II hyperbolic band (0.17 eV $< \hbar\omega <$ 0.20 eV) and interband transition region stands for potential channels of ultrahigh radiative heat fluxes.

The net heat flux can be modeled by fluctuational electrodynamics with a recursive transfer matrix method [2,10,26]. The net heat flux emitted by the InSb cell through vacuum gap is calculated by

$$Q = \frac{1}{4\pi^2} \int_0^\infty \hbar\omega[\psi(\omega, T_1, \mu_1) - \Theta(\omega, T_2)]d\omega \int_0^\infty \sum_{j=s,p} \xi_j(\omega, k_\parallel)k_\parallel dk_\parallel \tag{3}$$

Here, $\Theta(\omega, T) = [\exp(\hbar\omega/k_B T) - 1]^{-1}$ is the Bose-Einstein distribution, and $\psi(\omega, T, \mu) = \{\exp[(\hbar\omega - \mu)/k_B T] - 1\}^{-1}$ is the modified Bose-Einstein distribution with a given photon chemical potential, μ [2,27]. Note that $\xi_j(\omega, k_\parallel)$ represents the energy transmission coefficient from the InSb film to the upper region (the hBN film and the vacuum at the top), $k_\parallel = \sqrt{k_x^2 + k_y^2}$ is the magnitude of the parallel wavevector in the x-y plane, and subscript j represents either the transverse electric waves (s-polarization) or transverse magnetic waves (p-polarization). The energy transmission coefficient can be obtained from

$$\xi_j(\omega, k_\parallel) = \int_0^{h_1} \mathrm{Re}\left[i\varepsilon_1''(\omega, T_1)F(\omega, k_\parallel, z, h_1)\right]dz \tag{4}$$

The function F represents the solution of multilayer Green's function for the emission at the surface h_1 originated from position z, and $\varepsilon_1''(\omega, T_1)$ is the imaginary part of the electric permittivity of the TR cell. The detailed calculation procedures of the energy transmission coefficient in an anisotropic stratified medium are well-documented in Ref. [26]. The net photon flux emitted by the InSb film has a similar expression as the net heat flux, which can be written as

$$N = \frac{1}{4\pi^2} \int_{\omega_g}^\infty [\psi(\omega, T_1, \mu_1) - \Theta(\omega, T_2)]d\omega \int_0^\infty \sum_{j=s,p} \xi_j(\omega, k_\parallel)k_\parallel dk_\parallel \tag{5}$$

The detailed balance analysis is used to calculate the output power and device efficiency. The current can be obtained as

$$J(V) = J_{RR} - J_A - J_{SRH} = e[N(V) - G_A(V) - G_{SRH}(V)] \tag{6}$$

where e is the elementary charge. G is the nonradiative generation rate of the cell. Subscript RR, A and SRH represents radiative recombination, Auger process and Shockley-Read-Hall (SRH) process, respectively, which can be calculated using the following equations:

$$G_A(V) = C(n + p)(n_i^2 - np)h_1 \tag{7}$$

$$G_{SRH}(V) = \frac{1}{\tau}\frac{(n_i^2 - np)h_1}{n + p + 2n_i} \tag{8}$$

where C is the Auger coefficient and τ is the SRH lifetime of the free carriers; n and p are the electron and hole concentrations; and n_i is the intrinsic carrier concentration. Note that the carrier concentrations are also temperature-dependent and can be calculated using $np = n_i^2(T_1)\exp(\mu_1/k_B T_1)$.

To suppress Auger process, the InSb is chosen to be intrinsic with a thin-film structure. No high-level injection condition should be considered, so the spatial variation of photon chemical potential can be neglected for this thin-film TR device. Therefore, $\mu_1 = Ve$ [27]. The SRH lifetime is a defect-dependent property, which is assumed to be 98 ns [7].
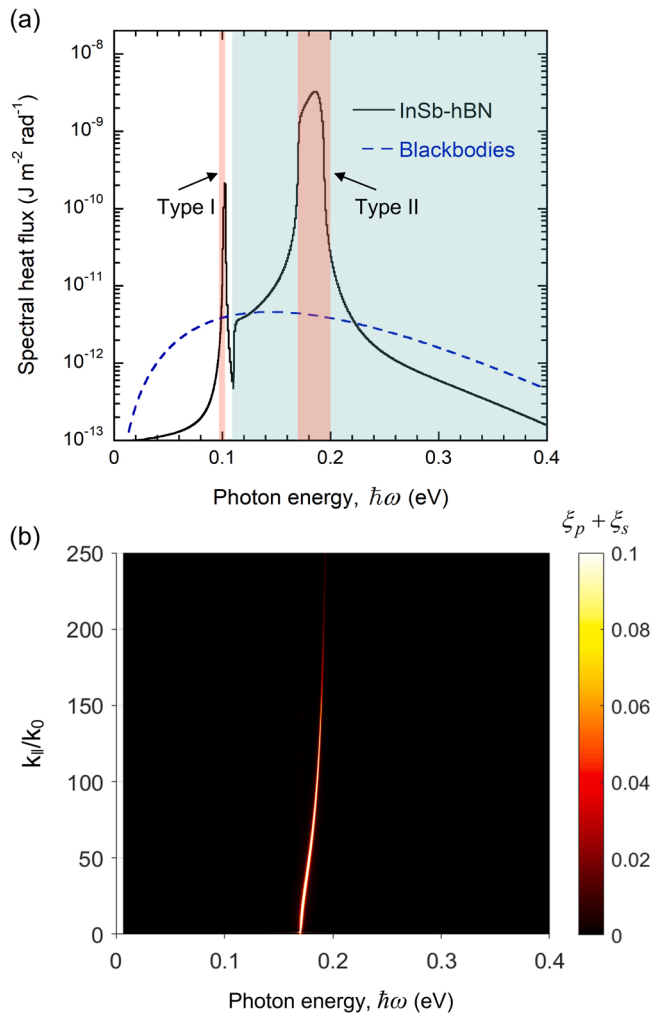
The output power per unit area and conversion efficiency are obtained by

$$P(V) = J(V)V \tag{9}$$

and

$$\eta(V) = P(V)/[P(V) + Q(V)] \tag{10}$$

The net emitted heat flux Q depends on the photon chemical potential, which is essentially a function of the applied voltage in this work.

(a)

(b)

Fig. 3. (a) Spectral heat flux of the near-field TR device and two blackbodies with the same temperatures, and (b) the contour plot of the transmission coefficient at $V = 0$ V.

3. Results and discussion

In order to analyze the mechanism resulting in this TR device, the spectral heat flux at the short-circuit scenario is shown in Fig. 3(a), where the temperatures of the hot and cold sides are fixed at $T_1 = 550$ K and $T_2 = 300$ K, respectively. The film and vacuum gap thicknesses are $h_1 = 50$ nm, $h_2 = 5$ nm, and $d = 10$ nm. These temperature and thickness values are used as default in this work unless otherwise indicated. The spectrum is divided into two regions: below bandgap energy (unshaded area) and above bandgap energy (blue shaded area). As we can see, most of the radiation energy concentrates at the peak above the bandgap energy. The total heat flux corresponding to the radiative recombination is 8.7 W/cm², while only 0.7% of total heat flux is emitted by InSb cell as parasitic heat (below bandgap energy), which cannot generate electricity. Therefore, this near-field TR device exhibits a nearly ideal heat flux spectrum, which is the key characteristic of a radiative energy converter with a high conversion efficiency. The spectral heat flux of two blackbodies at the same corresponding temperatures is also shown for comparison. Due to the coupling of HPhPs and interband transitions, the total heat flux is 18 folds of that for two blackbodies at the same temperatures. An enhancement on the output power due to near-field effect is expected and will be discussed in the later context. Two peaks of the spectral heat flux are corresponding to the two hyperbolic bands, which are shaded as red. The spectral heat flux starts to increase at bandgap energy (0.11 eV at 550 K) due to

(a)

(b)
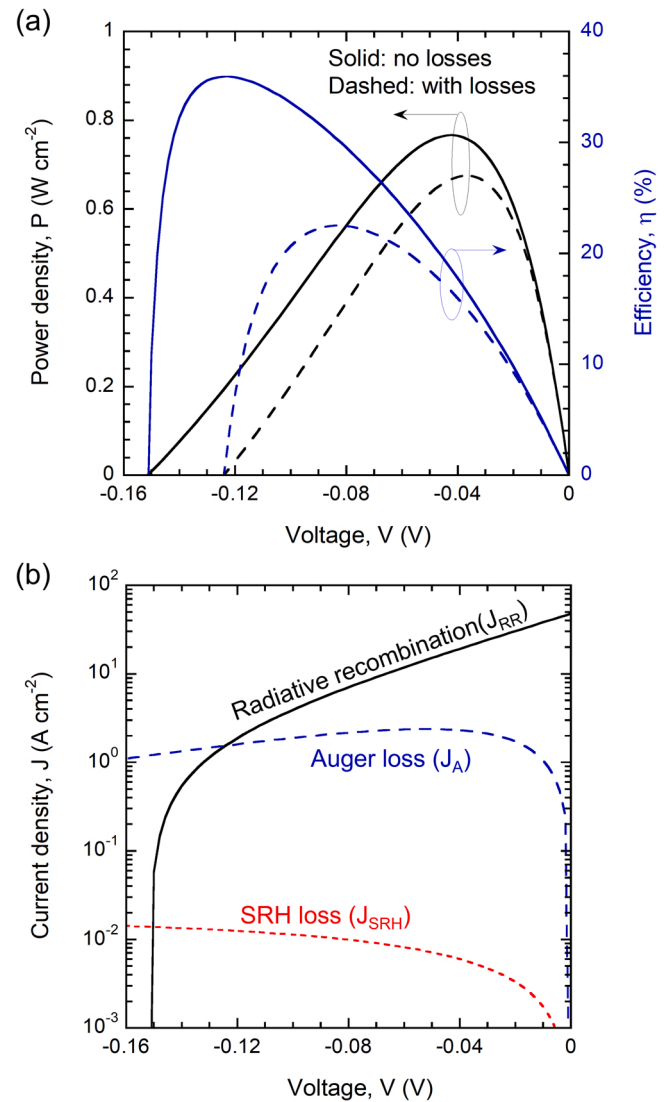
Fig. 4. (a) The power density and efficiency of the proposed TR device vs. the applied voltage with or without considering nonradiative losses. (b) Current densities vs. the applied voltage due to radiative recombination J_{RR}, Auger generation J_A ($C = 5 \times 10^{-27}$ cm⁶/s), and SRH generation J_{SRH}.

frustrated modes. As the photon energy reaches the hyperbolic band of hBN (0.17–0.2 eV), the spectral heat flux increases sharply as the HPhPs are excited. The contour plot of the transmission coefficient in Fig. 3(b) also indicates that the strong resonance occurs between the optical phonons and photons with large parallel wavevectors ($k_\parallel > m_1 k_0$). The other peak at around 0.1 eV is also due to the excitation of HPhPs for the type I hyperbolic band. However, the transmission coefficient at this hyperbolic band is much smaller than that of type II hyperbolic band due to the low absorption coefficient of InSb in this spectral range. Therefore, the parasitic emission is minimized so that the efficiency of this near-field TR device can reach close to the Carnot efficiency.

The calculated results for a near-field TR device using the default parameters are shown in Fig. 4 with or without considering losses. The ideal case without nonradiative losses is shown by the solid lines in Fig. 4(a). With the negative bias being built up by the thermally driven emission, the output power exhibits a maximum value of 0.77 W/cm² when $V = -0.042$ V, and the corresponding efficiency reaches to 18.5%. When the magnitude (absolute value) of the voltage bias increases, the radiative recombination is suppressed due to the low concentrations of free carriers. Nevertheless, the emitted power is also suppressed. Therefore, the efficiency of the TR device reaches its maximum at V
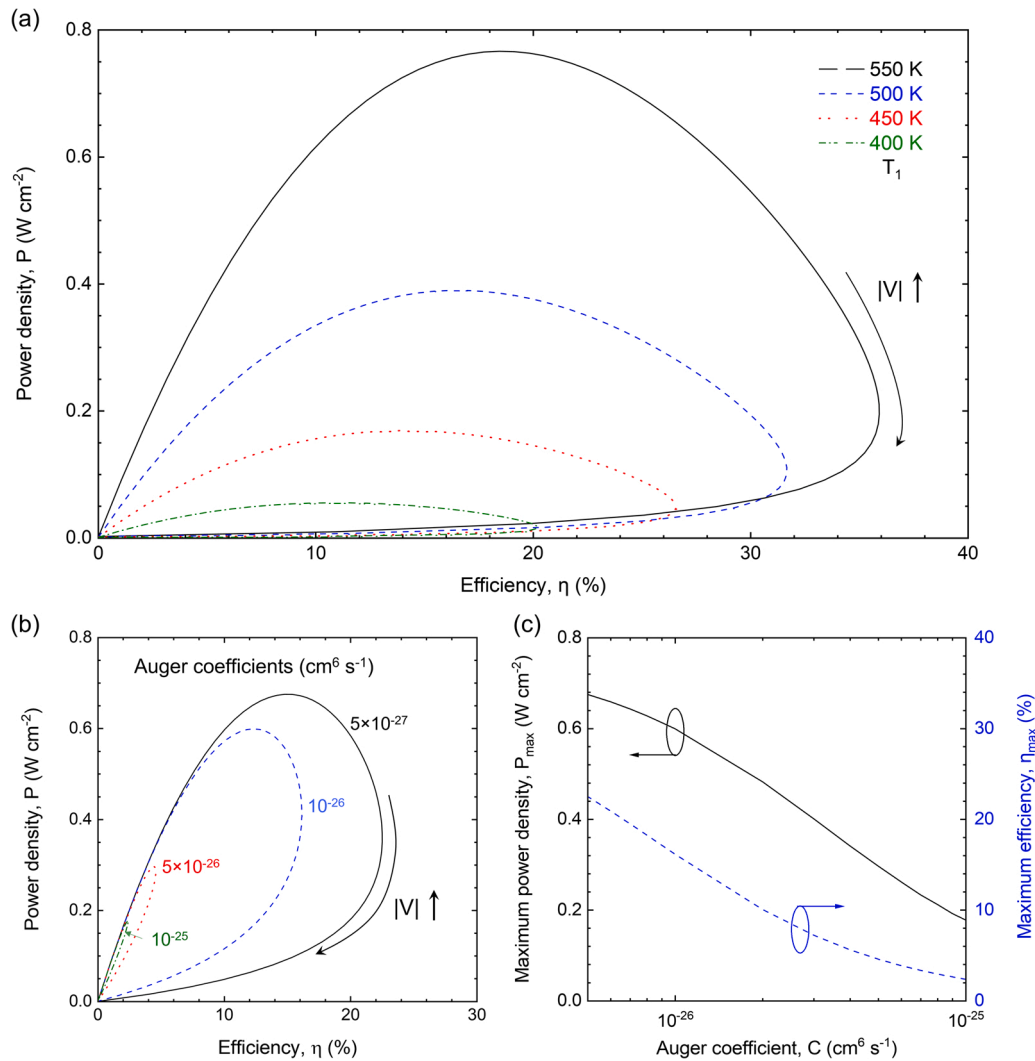
Fig. 5. (a) The power density and efficiency characteristics of the near-field TR device for different InSb cell temperatures, without considering the nonradiative losses. (b) The power density and efficiency characteristics for different Auger coefficients. (c) The maximum power density and maximum efficiency vs. Auger coefficient.

$= -0.124$ V to be 36%, which is almost 80% of the Carnot efficiency. The corresponding output power is much lower than the maximum but can still achieve a decent value of 0.19 W/cm². The mismatch between the voltages for the maximum output power and the maximum efficiency is because the efficiency is significantly affected by the emitted power as expressed by Eq. (10). The emitted power becomes comparable to the output power as the applied voltage decreases so that the efficiency reaches to its maximum.

To include the main mechanisms of nonidealities in the TR device, we consider Auger process and SRH process as the loss mechanisms with the values mentioned in the previous section. As shown by the dashed lines in Fig. 4(a), the maximum output power is reduced to 0.68 W/cm² and the maximum efficiency becomes 23%, which is about 51% of the Carnot efficiency. The free carriers at equilibrium are consumed by the radiative recombination, which makes the carrier concentrations lower than the equilibrium value. To recover the free carrier concentration to the original state, Auger and SRH processes are favorable in generating free carriers and consequently cause the nonradiative losses [28].

The current density corresponding to the radiative recombination, Auger process and SRH process are shown in Fig. 4(b). The short-circuit current density is 47.7 A/cm², which is revealed by J_{RR} at 0 V. The current generated by radiative recombination monotonically decreases as the applied voltage decreases. Auger generation rate is proportional

to $\exp(Ve/2k_B T_1) - \exp(3Ve/2k_B T_1)$. As the applied voltage decreases, J_A intersects with J_{RR} at $V = -0.124$ V, where the open-circuit voltage is obtained considering nonradiative losses. Compared to Auger generation, SRH generation causes little deterioration on the performance of the TR device with the chosen materials properties. The Auger coefficient is assumed to be 5×10^{-27} cm⁶/s by averaging the experimental values from the Ref. [29–31] with the temperature effect considered [32].

The power density and efficiency (*P-η*) curves are calculated at different temperatures of the InSb cell to investigate the cell temperature effect on the performance of the TR device. As shown in Fig. 5(a), the *P-η* curve starts at origin, where no voltage is applied. As the applied voltage goes towards a negative direction, both the power density and efficiency start to increase. The curve reaches to maximum power density first, and then the power density begins to decrease. However, the efficiency reaches a maximum at a more negative voltage than the power density, which has been discussed in Fig. 4(a). As the temperature of the TR cell decreases from 550 K to 400 K, smaller photon flux and higher bandgap energy indicate that fewer photons can be utilized to generate electricity. Consequently, the *P-η* curve shrinks as the temperature of the TR cell decreases. The maximum efficiency reduces from 36% to 20% and the maximum output power reduces from 0.77 W/cm² to 0.054 W/cm². The device efficiency remains at 80% of the Carnot efficiency as the cell
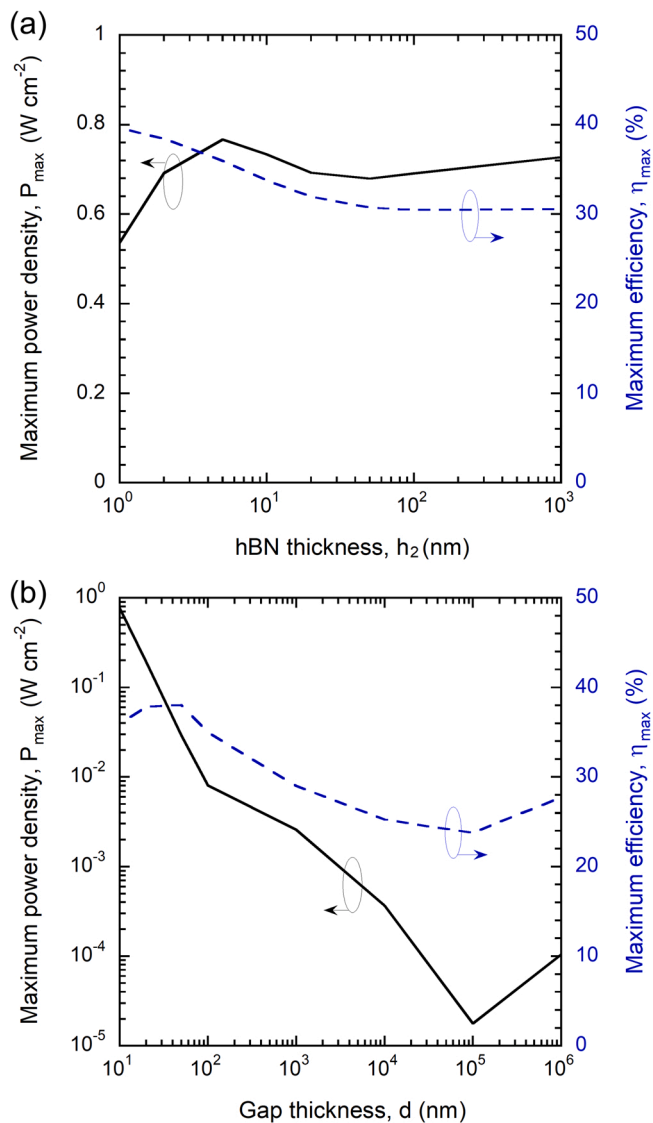
Fig. 6. The maximum power density and maximum efficiency vs. (a) the thickness of hBN sheet and (b) vacuum gap thickness. Note that nonradiative losses are not considered.

temperature decreases.

As discussed in Fig. 4(b), Auger generation is the dominant non-radiative loss in the TR device. Moreover, the Auger coefficient will increase as the temperature increases [32]. Therefore, a parametric analysis of Auger coefficient is further considered to design and optimize a real TR device. The *P-η* curves at different Auger coefficients are plotted in Fig. 5(b). According to Ref. [29], we choose the range of Auger coefficient in the parametric sweep to be 5×10^{-27} cm^6/s to 10^{-25} cm^6/s to include the temperature effect on the Auger coefficient. As the Auger coefficient decreases, the maximum power density is monotonically reduced from 0.68 W/cm^2 to 0.18 W/cm^2, and the maximum efficiency also decreases from 22.5% to 2.4%, which is shown in Fig. 5 (c). However, the maximum efficiency and output power can remain in a practical level if the Auger coefficient is suppressed lower than 10^{-26} cm^6/s. Therefore, the strategies for Auger suppression, including the use of the heterostructures or confined nanostructured cells [33,34], would be critical to make this near-field TR device a competitive energy conversion technology compared to other solid-state heat engines.

The thicknesses of the hBN sheet and vacuum gap are varied to investigate their effects on the performance of the proposed TR device. Auger generation and SRH generation are both volumetric processes so

that they are linearly proportional to the thickness of InSb. Also, the emission/absorption due to HPhPs occur at the skin depth of InSb cell. Therefore, the thickness of InSb is fixed at 50 nm to maximize the device performance by suppressing the nonradiative losses without deteriorating the photon exchange process. The variation range of the hBN sheet is chosen from 1 nm to 1 μm, which is shown in Fig. 6(a). The maximum output power exhibits oscillations as the hBN thickness increases due to the interference effect of hBN sheets [35]. The maximum output power occurs at $h_2 = 5$ nm, while the maximum efficiency decreases monotonically from 39.6% to 30.6% as the hBN thickness increases since more thermal energy is transferred by the photons with subbandgap energies. As shown in Fig. 6(b), the output power decreases significantly from 0.77 W/cm^2 to 0.0001 W/cm^2 as the vacuum gap thickness increases, which indicates a 7700-fold enhancement on the output power brought by the HPhPs at the nanoscale. The trend of efficiency is not monotonic because the reduction of emitted power is larger than that of maximum output power. When the vacuum gap thickness is 50 nm, the maximum efficiency can be 38.1%, which is 84% of the Carnot efficiency. For far-field operation, the proposed TR device can still achieve 27% efficiency.

4. Conclusions

In summary, a near-field TR device made of hBN and InSb is proposed and analytically demonstrated with a performance of > 80% of the Carnot efficiency. The HPhPs excited at nanoscales couple with the interband transition of InSb, which can enhance the maximum output power by 7700-fold over the far-field scenario. A comprehensive model is developed by combining the multilayer fluctuational electrodynamics of anisotropic materials and detailed balance approach, where the nonradiative processes are included. Suppressing Auger process in the InSb cell is critical for realizing this near-field TR device with a competitive performance. By tuning the hBN thickness, the maximum efficiency can reach 39.6%, which is 87% of the Carnot efficiency. This work offers a novel alternative to solid-state energy conversion technologies and opens a route to achieve low-grade heat recovery using thermoradiative cells at the nanoscale.

CRediT authorship contribution statement

Dudong Feng:, Conceptualization, Formal analysis, Methodology, Software, Writing – original draft, Writing – review & editing. **Xiulin Ruan:** Investigation, Resources, Writing – review & editing. **Shannon Yee:** Conceptualization, Investigation, Resources, Writing – review & editing. **Zhuomin Zhang:** Conceptualization, Funding acquisition, Investigation, Supervision, Writing – review & editing.

Declaration of Competing Interest

The authors declare that they have no known competing financial interests or personal relationships that could have appeared to influence the work reported in this paper.

Data Availability

Data will be made available on request.

Acknowledgements

References

[1] E.J. Tervo, E. Bagherisereshki, Z.M. Zhang, Near-field radiative thermoelectric energy converters: a review, Front. Energy 12 (1) (2018) 5–21, https://doi.org/10.1007/s11708-017-0517-z.

[2] Z.M. Zhang. Nano/Microscale Heat Transfer, 2nd ed., Springer Nature, Cham, 2020.

[3] R. Strandberg, Theoretical efficiency limits for thermoradiative energy conversion, J. Appl. Phys. 117 (5) (2015), 055105, https://doi.org/10.1063/1.4907392.

[4] P. Santhanam, S. Fan, Thermal-to-electrical energy conversion by diodes under negative illumination, Phys. Rev. B 93 (16) (2016), 161410, https://doi.org/10.1103/PhysRevB.93.161410.

[5] S.J. Byrnes, R. Blanchard, F. Capasso, Harvesting renewable energy from Earth's mid-infrared emissions, Proc. Natl. Acad. Sci. U.S.A. 111 (11) (2014) 3927–3932, https://doi.org/10.1073/pnas.1402036111.

[6] M. Ono, P. Santhanam, W. Li, B. Zhao, S. Fan, Experimental demonstration of energy harvesting from the sky using the negative illumination effect of a semiconductor photodiode, Appl. Phys. Lett. 114 (16) (2019), 161102, https://doi.org/10.1063/1.5089783.

[7] X. Zhang, Y.S. Ang, Jc Chen, L.K. Ang, Design of an InSb thermoradiative system for harvesting low-grade waste heat, Opt. Lett. 44 (13) (2019) 3354–3357, https://doi.org/10.1364/OL.44.003354.

[8] E.J. Tervo, W.A. Callahan, E.S. Toberer, M.A. Steiner, A.J. Ferguson, Solar thermoradiative-photovoltaic energy conversion, Cell Rep. Phys. Sci. 1 (12) (2020), 100258, https://doi.org/10.1016/j.xcrp.2020.100258.

[9] C. Lin, B. Wang, K.H. Teo, Z.M. Zhang, Performance comparison between photovoltaic and thermoradiative devices, J. Appl. Phys. 122 (24) (2017), 243103, https://doi.org/10.1063/1.5004651.

[10] D. Feng, STUDY OF THE PHOTON CHEMICAL POTENTIAL IN SEMICONDUCTOR RADIATIVE ENERGY CONVERTERS AT MICRO/NANOSCALES (Ph.D. dissertation), Georgia Institute of Technology, 2021.

[11] W.-C. Hsu, J.K. Tong, B. Liao, Y. Huang, S.V. Boriskina, G. Chen, Entropic and near-field improvements of thermoradiative cells, Sci. Rep. 6 (1) (2016) 34837, https://doi.org/10.1038/srep34837.

[12] B. Wang, C. Lin, K.H. Teo, Z.M. Zhang, Thermoradiative device enhanced by near-field coupled structures, J. Quant. Spectrosc. Radiat. Transf. 196 (2017) 10–16, https://doi.org/10.1063/1.5007036.

[13] A. Ghanekar, Y. Tian, X. Liu, Y. Zheng, Performance enhancement of near-field thermoradiative devices using hyperbolic metamaterials, J. Photonics Energy 9 (3) (2019), 032706, https://doi.org/10.1117/1.JPE.9.032706.

[14] C. Lin, B. Wang, K.H. Teo, Z. Zhang, Near-field enhancement of thermoradiative devices, J. Appl. Phys. 122 (14) (2017), 143102, https://doi.org/10.1016/j.jqsrt.2017.03.038.

[15] A. Narayanaswamy, G. Chen, Surface modes for near field thermophotovoltaics, Appl. Phys. Lett. 82 (20) (2003) 3544–3546, https://doi.org/10.1063/1.1575936.

[16] E.E. Narimanov, A.V. Kildishev, Naturally hyperbolic, Nat. Photonics 9 (4) (2015) 214–216, https://doi.org/10.1038/nphoton.2015.56.

[17] A. Poddubny, I. Iorsh, P. Belov, Y. Kivshar, Hyperbolic metamaterials, Nat. Photonics 7 (12) (2013) 948–957, https://doi.org/10.1038/nphoton.2013.243.

[18] R. Messina, P. Ben-Abdallah, Graphene-based photovoltaic cells for near-field thermal energy conversion, Sci. Rep. 3 (1) (2013) 1383, https://doi.org/10.1038/srep01383.

[19] R. Wang, J. Lu, J.-H. Jiang, Enhancing thermophotovoltaic performance using graphene-BN-InSb near-field heterostructures, Phys. Rev. Appl. 12 (4) (2019), 044038, https://doi.org/10.1103/PhysRevApplied.12.044038.

[20] O. Ilic, M. Jablan, J.D. Joannopoulos, I. Celanovic, M. Soljačić, Overcoming the black body limit in plasmonic and graphene near-field thermophotovoltaic systems, Opt. Express 20 (S3) (2012) A366–A384, https://doi.org/10.1364/OE.20.00A366.

[21] T.S. Moss, S.D. Smith, T.D.F. Hawkins, Absorption and dispersion of indium antimonide, Proc. Phys. Soc. Lond., Sect. B 70 (8) (1957) 776–784, https://doi.org/10.1088/0370-1301/70/8/307.

[22] P.Y. Liu, J.C. Maan, Optical properties of InSb between 300 and 700 K. I. Temperature dependence of the energy gap, Phys. Rev. B 47 (24) (1993) 16274–16278, https://doi.org/10.1103/PhysRevB.47.16274.

[23] G.W. Gobeli, H.Y. Fan, Infrared absorption and valence band in indium antimonide, Phys. Rev. 119 (2) (1960) 613–620, https://doi.org/10.1103/PhysRev.119.613.

[24] D. Feng, S.K. Yee, Z.M. Zhang, Near-field photonic thermal diode based on hBN and InSb films, Appl. Phys. Lett. 119 (18) (2021), 181111, https://doi.org/10.1063/5.0068775.

[25] A. Kumar, T. Low, K.H. Fung, P. Avouris, N.X. Fang, Tunable light–matter interaction and the role of hyperbolicity in graphene–hBN system, Nano Lett. 15 (5) (2015) 3172–3180, https://doi.org/10.1021/acs.nanolett.5b01191.

[26] T.J. Bright, X.L. Liu, Z.M. Zhang, Energy streamlines in near-field radiative heat transfer between hyperbolic metamaterials, Opt. Express 22 (S4) (2014) A1112–A1127, https://doi.org/10.1364/OE.22.0A1112.

[27] D. Feng, E.J. Tervo, D. Vasileska, S.K. Yee, A. Rohatgi, Z.M. Zhang, Spatial profiles of photon chemical potential in near-field thermophotovoltaic cells, J. Appl. Phys. 129 (21) (2021), 213101, https://doi.org/10.1063/5.0047241.

[28] J.A. Del Alamo, Integrated Microelectronic Devices: Physics and Modeling, Pearson, 2018.

[29] S. Marchetti, M. Martinelli, R. Simili, The InSb Auger recombination coefficient derived from the IR-FIR dynamical plasma reflectivity, J. Phys.: Condens. Matter 13 (33) (2001) 7363–7369, https://doi.org/10.1088/0953-8984/13/33/316.

[30] C.M. Ciesla, B.N. Murdin, C.R. Pidgeon, R.A. Stradling, C.C. Phillips, M. Livingstone, I. Galbraith, D.A. Jaroszynski, C.J.G.M. Langerak, P.J.P. Tang, M. J. Pullin, Suppression of Auger recombination in arsenic-rich $InAs_{1-x}Sb_x$ strained layer superlattices, J. Appl. Phys. 80 (5) (1996) 2994–2997, https://doi.org/10.1063/1.363157.

[31] L. Almazov, Properties of a high-density non-equilibrium plasma in InSb. Fizika i Tekhnika Poluprovodnikov (Physics and Technology of Semiconductors), 14(10) (1980) 1940–1946.

[32] J. Piprek, Semiconductor Optoelectronic Devices: Introduction to Physics and Simulation, Elsevier, 2013.

[33] G.G. Zegrya, A.D. Andreev, Mechanism of suppression of Auger recombination processes in type-II heterostructures, Appl. Phys. Lett. 67 (18) (1995) 2681–2683, https://doi.org/10.1063/1.114291.

[34] G.E. Cragg, A.L. Efros, Suppression of Auger processes in confined structures, Nano Lett. 10 (1) (2010) 313–317, https://doi.org/10.1021/nl903592h.

[35] X. Wu, C. Fu, Near-field radiative heat transfer between uniaxial hyperbolic media: Role of volume and surface phonon polaritons, J. Quant. Spectrosc. Radiat. Transf. 258 (2021), 107337, https://doi.org/10.1016/j.jqsrt.2020.107337.

Dr. Dudong Feng is a post-doctoral research fellow in the School of Mechanical Engineering and the Birck Nanotechnology Center at Purdue University. He received B.E. from Zhejiang University, and M.S. from Carnegie Mellon University. He completed his Ph.D. degree from Georgia Institute of Technology in 2021. He has authored and co-authored over 10 journal and conference papers. His research interests include near-field radiation with applications to radiative energy converters, first-principles calculation for materials screening, and photonic and polaritonic devices.

Dr. Xiulin Ruan is a professor in the School of Mechanical Engineering and the Birck Nanotechnology Center at Purdue University. He received his B.S. and M.S. in Engineering Thermophysics from Tsinghua University in 2000 and 2002, respectively. He received an M.S. in Electrical Engineering and Ph.D. in Mechanical Engineering from the University of Michigan at Ann Arbor, in 2006 and 2007 respectively. His research interests are in atomistic simulations of thermal transport for sustainable energy and electronics thermal management applications; scalable fabrication and additive manufacturing of nanocomposites and devices for radiative cooling; machine learning, optimization, and high throughput design.

Dr. Shannon Yee is an Associate Professor at the G.W.W. School of Mechanical Engineering at the Georgia Institute of Technology. Dr. Yee joined Georgia Tech in 2014 directly from his PhD studies at the University of California Berkeley. In 2010, he joined the US. Dept. of Energy's Advanced Research Projects Agency for Energy (ARPA-E) during its inaugural year as the first ARPA-E Fellow. Dr. Yee completed his MS in Nuclear Engineering in 2008 and his BS in Mechanical Engineering in 2007, both from The Ohio State University. In 2008, he was awarded a prestigious Hertz Fellowship.

Dr. Zhuomin Zhang holds the J. Erskine Love, Jr. Professorship in mechanical engineering at Georgia Institute of Technology. He received B.S. and M.S. from the University of Science and Technology of China and Ph.D. from MIT. His research interests are in nanoscale thermal radiation for energy harvesting. He has published a book Nano/Microscale Heat Transfer (2nd ed. 2020) and co-authored over 200 journal articles. Dr. Zhang is Fellow of ASME, AAAS, and APS, and a winner of the ICHMT Hartnett-Irvine Award (2010; 2019), ASME Heat Transfer Memorial Award (2015), AIAA Thermophysics Award (2021), ASME Yeram S. Touloukian Award (2021).